PHOTONICS Research

Single-/fused-band dual-mode mid-infrared imaging with colloidal quantum-dot triple-junctions

SHUO ZHANG,[1,†] GE MU,[1,†] JIE CAO,[1,2,3] YUNING LUO,[1] QUN HAO,[1,2,3,4] MENGLU CHEN,[1,2,3,5] YIMEI TAN,[3] PENGFEI ZHAO,[1] AND XIN TANG[1,2,3,6]

[1]*School of Optics and Photonics, Beijing Institute of Technology, Beijing 100081, China*
[2]*Beijing Key Laboratory for Precision Optoelectronic Measurement Instrument and Technology, Beijing 100081, China*
[3]*Yangtze Delta Region Academy of Beijing Institute of Technology, Jiaxing 314019, China*
[4]*e-mail: qhao@bit.edu.cn*
[5]*e-mail: menglu@bit.edu.cn*
[6]*e-mail: xintang@bit.edu.cn*

Image data acquired with fused multispectral information can be used for effective identification and navigation owing to additional information beyond human vision, including thermal distribution, night vision, and molecular composition. However, the construction of photodetectors with such capabilities is hindered by the structural complexity arising from the integration of multiple semiconductor junctions with distinct energy gaps and lattice constants. In this work, we develop a colloidal quantum-dot dual-mode detector capable of detecting, separating, and fusing photons from various wavelength ranges. Using three vertically stacked colloidal quantum-dot homojunctions with alternating polarity, single-band short-wave infrared imaging and fused-band imaging (short-wave and mid-wave infrared) can be achieved with the same detector by controlling bias polarity and magnitude. The dual-mode detectors show detectivity up to 8×10^{10} Jones at the fused-band mode and 3.1×10^{11} Jones at the single-band mode, respectively. Without image post-processing algorithms, the dual-mode detectors could provide both night vision and thermal information-enhanced night vision imaging capability. To the best of our knowledge, this is the first colloidal quantum-dot detector that can achieve such functionality. The operation mode can be changed at a high frequency up to 1.7 MHz, making it possible to achieve simultaneously dual-mode imaging and remote temperature sensing.   © 2022 Chinese Laser Press

https://doi.org/10.1364/PRJ.458351

1. INTRODUCTION

Extensive efforts have been made in the infrared ranges with the desire to achieve multiband or hyperspectral imaging. Going beyond human vision capability, infrared can provide objects' important information such as molecular composition and thermal distribution. For better target recognition and identification, there are strong demands for combining images from different spectral bands, which is also known as spectral image fusion technology [1]. This image from fused spectral bands can provide a more accurate understanding of the surrounding information compared to single spectral data. Despite continuous efforts on sophisticated fusion algorithms [2–4], registration error inevitably presents due to the mismatch of pixel size, array size, and optical imaging axis between separate imagers.

The simple solution to this problem would be an imager that responds to distinct spectral ranges and fuse signals on the pixel level. However, the spectral sensing ranges of imagers are mainly defined by their materials (e.g., Si for 0.4–0.7 nm at

visible, InGaAs for 1.5–1.7 μm at short-wave infrared, and HgCdTe for 3–12 μm at mid-infrared) and combination of different materials into the same pixel vertically or horizontally is hindered by the lattice mismatch and incompatibility between fabrication processes.

As an alternative to epitaxial semiconductors, colloidal quantum dots (CQDs), over the past years, have been extensively explored for their unique properties such as size-tunable optical features and the ease of fabrication as solution-processable materials [5]. With continuous advancements in synthesis, the sensing ranges of CQDs have been gradually extended to access mid-infrared [6,7] with state-of-the-art device performance rivaling to their counterparts of bulk semiconductors. Among colloidal nanomaterials, mercury chalcogenides (HgX, X represents S, Se, Te) CQDs have demonstrated, so far, the highest spectral tunability. Short-wave infrared (SWIR) photovoltaic detectors with detectivity D^* up to 10^{11} Jones on rigid/flexible substrates [8], and mid-wave infrared (MWIR) photovoltaic detectors with background-limited infrared photodetection performance [9,10]

have all been achieved. Despite excellent device performance, fusing different infrared spectral bands into a single CQDs detector still faces technological obstacles, as prior research mainly focused on single-color detection [11–13] or emission [14] applications.

To address such technological challenges and meet the growing demands for fused multispectral infrared imaging, we propose the development of a dual-mode colloidal quantum-dot infrared detector, which provides unprecedented bias-dependent single-band SWIR imaging mode and fused-band SWIR/MWIR mode. The SWIR mode provides details of the scene such as visible light, while the fused SWIR/MWIR mode adds thermal information directly to the SWIR image on the detector level. Our results show that a triple-junction structure arranged in alternating polarity is the key to fused response. The dual-mode detectors show D^* above 10^{11} Jones at the SWIR mode and 10^{10} Jones at the fused mode, rivaling epitaxial detectors at similar operation wavelength [15]. To the best of our knowledge, this is the first CQDs detector that can achieve such functionality. Using a scanning imaging system, high-resolution dual-mode imaging with an effective frame rate of over 5 kHz has been demonstrated, highlighting the potential of CQDs technology in the development of next-generation infrared imagers.

2. MATERIALS AND METHODS

A. Device Physics and Operation Principle

The study of infrared CQDs starts from photoconductive and single-junction photovoltaic device configuration, which clearly exhibits no spectral selectivity or fusion ability. Inspired by the band engineering of epitaxial semiconductors [16] (HgCdTe, quantum wells, Type II superlattice), a two-color CQDs detector with vertically stacked "back-to-back" diode configuration was introduced and demonstrated bias-tunable spectral response [17]. However, they still output single-band data at a fixed bias and require post-processing for image fusion. It is true that a three-terminal detector with a third middle common contact could possibly output images from two spectral bands simultaneously, but that inevitably increases structural complexity and cost of readout circuits.

The difficulty in fused response lies in the need that photocurrents from different spectral bands need to be combined either in series or in parallel with high efficiency. Our initial attempts include (1) the combination of a photoconductive SWIR layer with photovoltaic MWIR junction, (2) photovoltaic junction with mixed SWIR/MWIR CQDs solution, (3) parallelly stacked MWIR and SWIR junction, and (4) tandem SWIR/MWIR configuration. Despite that fused-band spectral response was indeed measured, they all showed low detectivity below 10^8 Jones, which is much inferior to single-band SWIR or MWIR photodiodes. We found that such structures suffer from low quantum efficiency, large leakage currents, high spectral cross-talking, and adverse interfacial carrier transport mechanism. Detector-level fused spectral response from CQDs with two different energy gaps remains unsolved and it seems that elaborated band and interface engineering are the key prerequisites for such functionalities.

To realize efficient fused-band response, we designed a new device architecture by stacking three rectifying colloidal

quantum-dot homojunctions, as shown in Fig. 1(a). The top SWIR photodiode and bottom MWIR photodiode have the same polarity. An SWIR photodiode with opposite polarity is sandwiched in the middle, which plays a central role in the fused-band operation and provides an additional single-band response mode. When the triple-junction detector works in the fused-band mode, the middle SWIR diode is turned off and provides an essential interfacial charge transport channel for photogenerated carriers. By changing the bias direction, both the top SWIR photodiode and bottom MWIR photodiode are closed. The triple-junction detector then outputs single-band SWIR signals. With two terminals, such detectors allow unprecedented bias-polarity-dependent dual-mode operation. The construction of the dual-mode detectors starts from the colloidal synthesis of HgTe CQDs that access the SWIR (4000–6000 cm^{-1}) and MWIR (2000–3333 cm^{-1}) regions [Fig. 1(b)]. Benefitting from their solution-processability, different-sized CQDs layers can be added consecutively by simple spin-coating or spray deposition [18], which allows advantageous wafer-scale fabrication of photodetectors directly on silicon or sapphire substrates. The cross-sectional transmission electron microscopy image of the dual-mode detector is shown in Fig. 1(c). The inset is a microscope image of the dual-mode detectors whose area is 200 µm × 200 µm defined by the overlap between the top gold electrode and the bottom ITO electrode. Rectifying junctions and built-in electric fields were precisely induced in the targeted region by fixing Ag$^+$ dopants as hole donors [17].

B. Device Fabrication

The synthesis of HgTe CQDs and Ag$_2$Te nanocrystals is similar to those reported in Ref. [17]. The dual-mode infrared detectors were fabricated on a sapphire substrate. 100 nm ITO film was deposited on the sapphire substrate by magnetron sputtering and annealed at 300°C for 15 min. Then, 3-mercaptopropyltrimethoxysilane was used to treat the substrate for 1 min to increase the adhesion between the substrate and the CQDs. The active layer was fabricated by layer-by-layer spin-coating of nanomaterials. First, the MWIR HgTe CQDs solution was spin-coated into a film with a thickness of about 300 nm, and the spin-coating parameter was 800 r/min for 60 s. Each layer of spin-coated CQDs requires ligand-exchange with ethanedithiol (EDT)/HCl/isopropanol (IPA) (1:1:50 by volume) solution for 10 s, rinsed with IPA and dried with N$_2$. Next, a layer of Ag$_2$Te nanocrystals was spin-coated on the HgTe CQDs as the p-dopant at 3000 r/min for 60 s, followed by HgCl$_2$ (10 mmol/L) treatment for 10 s. The second layer of Ag$_2$Te nanocrystals was deposited on the first Ag$_2$Te nanocrystals layer in the same way but without HgCl$_2$ treatment. Then, a layer of SWIR HgTe CQDs was spin-coated onto it. SWIR HgTe CQDs/Ag$_2$Te nanocrystals mix layers were treated with HgCl$_2$ solution. Multilayer SWIR CQDs by spin-coating were used to build up a 400 nm film, and each layer was treated with EDT/HCl/IPA (1:1:50 by volume) solution for 10 s. Afterward, two layers of Ag$_2$Te nanocrystals were spin-coated at 3000 r/min for 60 s, and each layer of Ag$_2$Te nanocrystals was treated with HgCl$_2$ (10 mmol/L) for 10 s. Finally, 10 nm Au was deposited as the top contact.
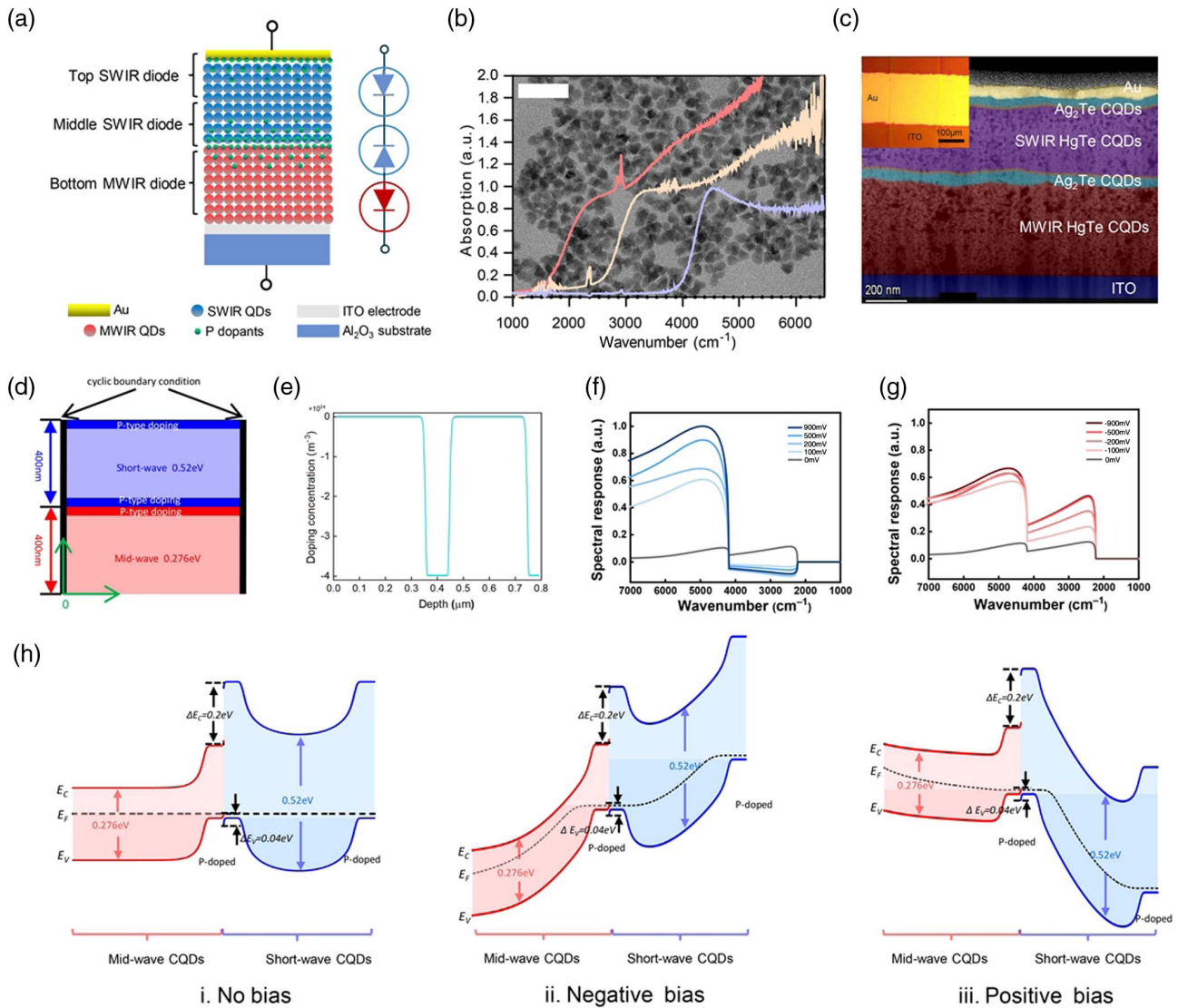
Fig. 1. Infrared spectral fusion technology. (a) Illustration of dual-mode colloidal quantum-dot photodetectors and equivalent circuits of triple-junction structure. (b) Transmission electron microscopy and absorption of HgTe colloidal quantum dots with various sizes. The scale bar is 10 nm. (c) Cross-sectional transmission electron microscopy image of the dual-mode detectors. Inset is a microscope image of the dual-mode detectors whose area is defined by the overlap between the top gold electrode and the bottom ITO electrode. (d) The simulation model of the HgTe CQDs dual-mode infrared detector. (e) Distribution of doping concentration. (f), (g) The simulation spectral responses of the dual-mode infrared detector under negative bias and positive bias. (h) Simulated energy band diagram of dual-mode triple-junction photodetectors under zero, negative, and positive bias voltage.

C. Photoresponse Characterization

The detector was placed in a cryostat for performance characterization. Responsivity was measured using a calibrated blackbody source at 600°C. The photon flux on the detector was determined by the area of the detector, the area of the blackbody, the distance between the detector and the blackbody, and the spectrum of the blackbody radiation. The photocurrent was amplified first by a preamplifier (Femto DLA-200) and the noise was measured with a spectrum analyzer.

D. Experimental Processes of Scanning Imaging

The single-pixel scanning system consists of imaging objects, an infrared lens, motorized *XY* linear stages, a dual-mode

photodetector, an amplifier, a data acquisition card, and software. The lens is mounted on the motorized *XY* stage, the imaging object is located in ∼50 cm away from the lens, and the detector is placed at the focus of the lens on the other side. Controlled by a motorized stage, the lens is scanned over a 25 mm × 25 mm area. Moreover, two displacement sensors are installed on the arms of the motorized stage to obtain the real-time position of the lens. As the projected image of the object moves over the photodetector, both the amplified photocurrent of the photodetector and the corresponding position signal are sampled by the data acquisition card (sampling frequency = 5 kHz). The single/fused infrared image of the object can be obtained after image reconstruction.

3. RESULTS AND DISCUSSION

A. Device Simulation

To investigate the device physics and operation mechanism, the structure, energy band, and performance of the dual-mode detectors were simulated with the finite element analysis method using the semiconductor module and wave optics module. Figure 1(d) shows the schematic diagram of the simulation model, in which the lower left corner is the origin of coordinates, and the two sides are periodic boundary conditions. The mid-wave HgTe CQDs and short-wave HgTe CQDs both with a thickness of 400 nm were stacked vertically with bandgaps of 0.52 eV and 0.27 eV. P-type doping was introduced at the top of the mid-wave HgTe CQDs layer and at the bottom and top of the short-wave HgTe CQDs layer. Figure 1(e) shows the distribution of doping concentration. The spectral responses of the dual-mode infrared detector under different bias voltages are shown in Figs. 1(f) and 1(g). The device shows a short-wave and mid-wave fusion response under negative bias voltage and the responsivity increases with the increase of bias voltage. However, only strong short-wave response is shown under positive bias. It was in good agreement with the experimental results. The simulated energy diagram of a dual-mode detector is illustrated in Fig. 1(h). The results clearly showed that with the middle p-doping layer between SWIR CQDs and MWIR CQDs, the Fermi level near the interface was collectively shifted to the valence band which resulted in a reduced energy barrier for hole transportation [the first row of Fig. 1(h)]. Compared with other structures without the middle SWIR diode, ΔE_v in a dual-mode detector with triple junctions can be reduced to 0.04 eV. On the side of the conduction band, the energy barrier ΔE_c is ~0.2 eV and this substantial electron energy barrier facilitates photogenerated electron flow from SWIR CQDs to MWIR CQDs and blocks the diffusion current in the opposite direction. When the SWIR CQDs side is negatively biased, the middle SWIR diode is turned off and photocurrents flow from the MWIR CQDs to SWIR CQDs, which matched well with the interfacial energy barriers [the second row of Fig. 1(h)]. Therefore, under negative bias, the dual-mode detector works in the fused-band mode. It is worth noting that such configuration may have similarities with structures of tandem solar cells. However, a tandem structure would require a precise photocurrent balance between two diodes [11,19–21]. The interfacial charge recombination layer, light absorption coefficient, and film thickness have all to be carefully designed to avoid loss of photocurrent. For photodetection of the light source with an unknown spectrum or changing features of spectral emission, such photocurrent balance is almost impossible to be achieved. However, our triple-junction structures, in the fused-band mode, have no such limitation since carriers generated in one CQDs diode, as driven by built-in potentials, can move freely to the other side and be collected, favored by the addition of a middle p-doping layer. Compared with the tandem structure without the middle SWIR diode, the D^* of triple-junction detectors showed 3 orders of magnitude improvement. With the well-designed energy band configuration, selective separation, fusion, and access to targeted spectral bands were enabled.

B. Characterization of Dual-Mode Operation

The dual-mode detectors were mounted in a cryostat and cooled down to ~80 K with liquid nitrogen to reduce thermally activated carriers. With a Michelson interference measurement setup, the spectral response was characterized with a heated globar as the light source. The selective dual-mode detection performance is clearly shown in Figs. 2(a) and 2(b). Consistent with the prediction by simulated energy band diagram, the detectors indeed showed bias-tunable dual-mode photoresponse performance. When the top Au contact is positively biased above 100 mV, SWIR response with cutoff wavelength at 2.5 μm (4000 cm⁻¹) is achieved with negligible spectral cross-talking from MWIR CQDs. With negative bias polarity, the spectral response contribution from the MWIR range increases rapidly with the magnitude of bias voltage. The two spectral peaks evidentiate fused response, highlighting the advantages of SWIR/MWIR fused mode over single-band SWIR or MWIR detectors.

The simulated energy band diagram suggested efficient photocarriers transportation from one diode without the need for current balance to the other side of detectors. This is experimentally confirmed by measuring photoresponse to chopped SWIR light, MWIR light, and SWIR and MWIR light. The sum of photocurrents from SWIR and MWIR light approximates the photocurrents under the illumination of both SWIR and MWIR, which is clear evidence that photocarriers generated inside the detector can be generated, add, and move freely [Fig. 2(c)]. To calculate the responsivity and detectivity, the I-V characteristics of the dual-mode detector were measured with a calibrated blackbody with a temperature of 600°C at various distances [Fig. 2(d)]. The photoresponse in the fused-band mode is around 3 times higher than in single-band SWIR mode, which matches the spectral radiation of the light source. We noticed that at ~26 mV, the dual-mode detectors can be completely shut down by offsetting the internal built-in potentials, as shown in the inset of Fig. 2(d).

For infrared photodetectors, detectivity is the most important figure of merit as it is associated with the signal-to-noise ratio. The D^* of the HgTe CQDs photodiode can be modeled as

$$D^* = \frac{\sqrt{A \cdot \Delta f}}{I_n} \Re, \qquad (1)$$

where A is the sensing area, Δf is the bandwidth, I_n is the noise spectral density, and $\Re$ is the responsivity, and responsivity is calculated as

$$\Re = \frac{I_{ph}}{P}, \qquad (2)$$

where I_{ph} is the photocurrent, and P is the input optical power, which is estimated by the temperature, distance between the detector and light source, and detector area. The bias-dependent responsivity and detectivity D^* are shown in Fig. 2(e). At optimal conditions, the detectivity in the fused mode and single-band mode reaches up to 4×10^{10} Jones and 1.5×10^{11} Jones, respectively. The single mode and fused mode of the photodetector in our work are sensitive to SWIR and SWIR/MWIR, respectively. MWIR HgTe CQDs have narrower bandgap than SWIR CQDs and thermal carrier density
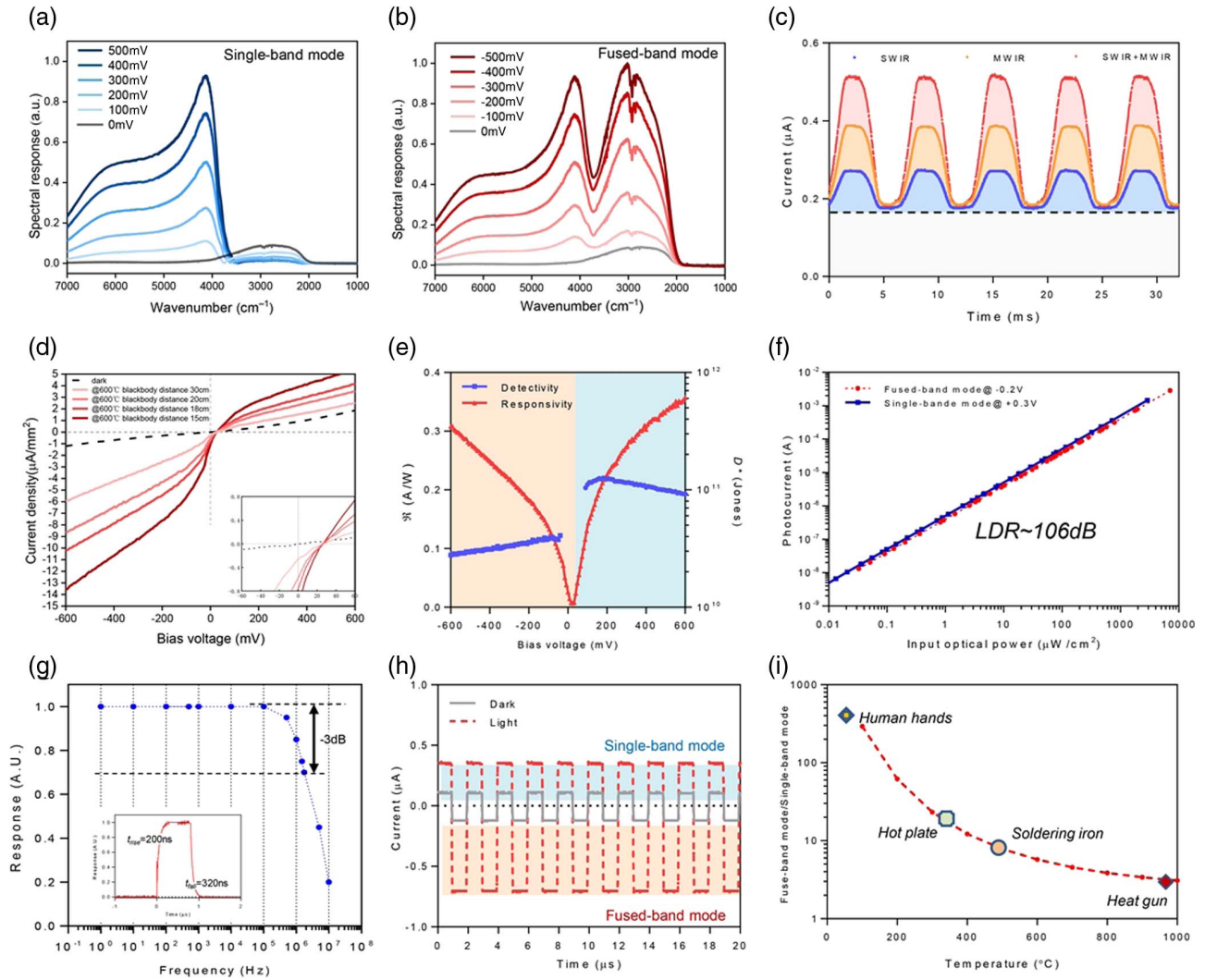
Fig. 2. Characterization of dual-mode detectors. Bias-dependent spectral response under (a) positive and (b) negative bias voltages. (c) Pulsed photoresponse to short-wave infrared, mid-wave infrared, and mixed illumination. (d) *I-V* characteristics of the dual-mode detector under blackbody irradiation at various distances. (e) Bias-dependent responsivity and detectivity of a dual-mode photodetector. (f) Linear dynamic range measurement of dual-mode detectors in the single-band mode and the fused-band mode. (g) Frequency response measurement of dual-mode detector. The inset is the measured response time of the dual-mode detector. (h) Photoresponse of the dual-mode detector biased with a positive and negative square wave at the frequency of 500 kHz. (i) Measured fused-band to single-band response ratio. The red dashed line is the measured ratio with a calibrated blackbody.

is higher in MWIR CQDs, resulting in larger thermal noise (Johnson noise) in the MWIR photodiode. Considering thermal noise is the main noise source in a photovoltaic device, the fused mode has larger noise than the single mode. Therefore, the detectivity of the fused mode is lower than that of the single-band mode. As an important parameter that reflects the property of converting the incident photon into an electron, external quantum efficiency (EQE) is defined as

$$\text{EQE} = \Re \frac{h\upsilon}{e}, \tag{3}$$

where $\Re$ is responsivity, h is Planck constant, υ is the corresponding frequency of cutoff wavelength, and e is the elementary electron charge. The EQEs of SWIR single mode and SWIR/MWIR fused mode are 15% and 11%, respectively.

Besides quantum efficiency, responsivity, and detectivity, linear dynamic range (LDR) and response time are two other important figures of merit for photodetectors. LDR is defined as the linear light intensity dependence of the photocurrent and is calculated as

$$\text{LDR} = 20 \times \log \frac{P_{\max}}{P_{\min}}, \tag{4}$$

where $P_{\max}$ and $P_{\min}$ are the upper and lower limits of the optical power in a particular range. By changing the temperature of the blackbody light source and the distance between the detector and the source, the optical light intensity can be changed, and the dual-mode detectors showed impressive LDR up to 100 dB in both single-band and fused-band modes [Fig. 2(f)]. For response time, generally, it is defined as the time for the

photocurrent to increase/decrease from 10%/90% to 90%/10% of the peak when the photocurrent arrives at a stable state after accepting/removing illumination. Using pulsed laser, the measured rise and fall times of the dual-mode detector are ~200 and 320 ns in both the single-band mode and the fused-band mode, implying that the two operation modes can be alternatingly changed at high speed up to 1.7 MHz [Fig. 2(g)].

By modulating the bias voltage, the SWIR and fused SWIR/MWIR signals can be read sequentially during a short time interval. The representative modulated photoresponses are shown in Fig. 2(h). The orange and blue shaded areas denote the magnitude of MWIR and SWIR signals, from which the single-band/fused-band response ratio can be calculated. The advantages of dual-mode detection are obvious. Unlike a single-band detector, such a dual-mode detector can precisely determine objects' temperature based on their emission spectrum. This method is independent of the magnitude of optical power or distance between the detector and the measured objects. As shown in Fig. 2(i), based on the calibrated fused-band mode/single-band mode signal ratio with a blackbody, the temperature of human hands, hotplates, soldering irons, and heat guns can be measured, highlighting the fact that the dual-mode detector can be used for absolute and remote temperature measurement. The blackbody curve is measured and calculated by using the blackbody as the light source. The ratio of photocurrents between the single-band mode and fused-band mode was recorded as the temperature of the blackbody changed.

It is true that bias-dependent dual-band detectors have been demonstrated by using two-dimensional materials [22–24], perovskites [25], and organic junctions [26], and excellent performance with detectivity above 10^{11} Jones has been demonstrated. However, the sensing ranges in prior studies mainly focused on visible and near-infrared below 1.5 μm and different detection spectral ranges can only be sequentially accessed with modulated bias voltages. Our colloidal quantum-dot dual-mode detector demonstrated, so far, the only detector that can give fused-band response in the mid-infrared regions.

C. Dual-Mode Infrared Imaging

The dual-mode operation enables our detectors with functionalities of both night vision and thermal imaging-enhanced night vision capability. To give a visual demonstration, the dual-mode detectors were integrated with a single-pixel scanning system for infrared imaging [Fig. 3(a)]. As the projected images scanned over the detectors, the photocurrents were amplified and recorded by a high-speed acquisition card at a sampling rate of 5 kHz.

As shown in Fig. 3(b), two soldering irons with the temperatures of 200°C and 25°C were imaged. When positively biased, the detector works in the single-band SWIR mode and the two soldering irons, including the one blocked behind a silicon wafer, were clearly captured with a tungsten lamp as the light source. By flipping the polarity of bias voltage, the detector works in the SWIR/MWIR fused mode. Without external light, the fused-mode detector can sense the thermal emission from objects and give the thermal distribution of the scene, in which only the "hot spot" on the soldering iron is noticeable. These results further confirmed the advantageous

feature that no photocurrent balance is needed for the triple-junction structure between two different sensing bands. After adding the external tungsten light, the fused-band detectors can spontaneously add the signal from two different bands and output fused photocurrent. As shown in the fourth row of Fig. 3(b), both MWIR thermal information and SWIR reflected image were captured.

As shown in Fig. 3(c), two cups of water with different temperatures were also imaged and showed consistent phenomena. It is worth noting that obscure silicon wafers can be seen through, and transparent water is black in SWIR images, highlighting the potential for SWIR in the application of semiconductor inspection and chemical analysis.

The noise equivalent temperature difference (NETD) is measured with two cups above. The NETD is defined as

$$\text{NETD} = \frac{\Delta T}{\Delta I_s / I_n}, \qquad (5)$$

where ΔT is the temperature between two cups (set to be 55°C), ΔI_s is the measured difference between the surface of cups, and I_n is the RMS noise of the detector. The calculated NETD is ~36 mK, demonstrating the high stability and low noise of the dual-mode imager.

D. Spectral and Spatial Light Manipulation for Enhanced Performance

Optical manipulation with plasmonic metallic structures [27,28], photonic crystals [29,30], meta-surfaces, and immersion lenses has been widely used in photodetectors to boost device performance by increasing light absorption. Usually, responsivity and quantum efficiency can be improved by near-field enhancement or light concentration. However, such structures are not suitable for a multispectral infrared detector or our dual-mode detectors. The first problem is that such configurations often give narrow spectral enhancement wavelength and cannot achieve improvements over the multiwavelength or broadband spectrum. More importantly, if the optical enhancement relies on near-field effects within sub-wavelength regions, it is not suitable for multiband or multimode photodetectors with layered functional structures where the localized light manipulation cannot spatially reach the layered sensing areas.

To further improve our device performance, we integrated the dual-mode detector into a well-designed resonance cavity which can spectrally and spatially match the light distribution inside the detectors with the triple sensing junctions. The detectivity and spectral selectivity can be improved at the same time. The resonant cavity is in Fabry–Perot configuration by simply adding an optical spacer and highly reflective gold mirror under the dual-mode detectors, as shown in Fig. 4(a). In a typical dual-mode detector, the thicknesses of SWIR and MWIR CQDs layers are both around 400 nm. The absorption edges were set to be 2.25 and 4 μm, respectively. As shown in the simulated light absorption distribution mapping in Fig. 4(b), with correct spacer thickness, the light absorption can be tuned to spatially match the depletion region of the junctions. For light with a wavelength of 2.25 μm, the maximum absorption region is near the top and bottom areas of SWIR CQDs, where strong built-in potentials are induced to separate photocarriers. For light with a wavelength of
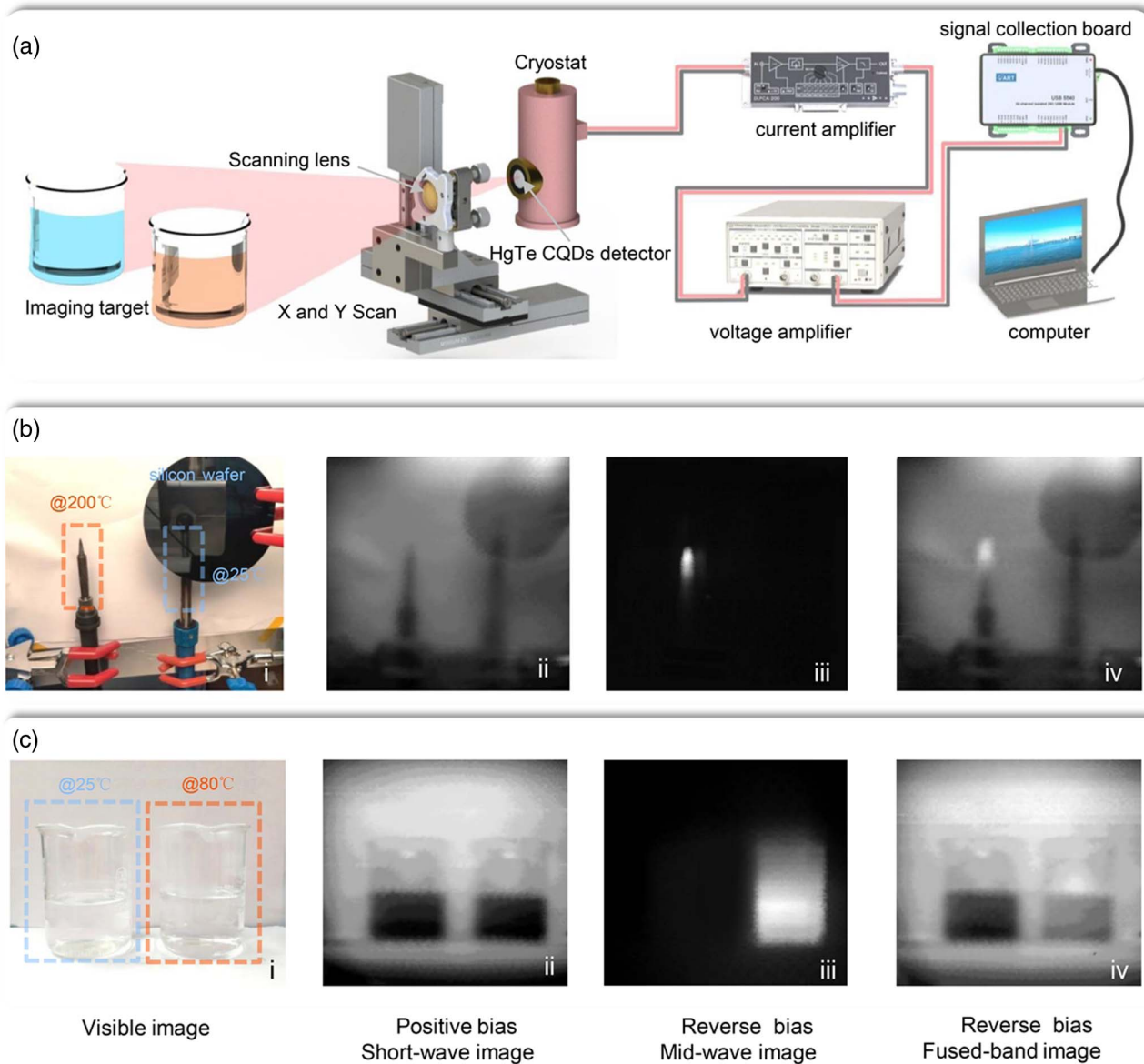
Fig. 3. Dual-mode infrared imaging. (a) Illustration of single-pixel scanning imaging setup. (b) Visible image, short-wave infrared, mid-wave infrared, and fused-mode images of two soldering irons. (c) Visible image, short-wave infrared, mid-wave infrared, and fused-mode images of two cups of water.

4 μm, the overall absorption across the whole sensing region was also notably enhanced. Therefore, the spatial and spectral modulation of light distribution inside the dual-mode detectors leads to enhanced light absorption and the spectral absorption enhancement can be tuned by optical spacer thickness. This is confirmed by both simulation and experimental results [Figs. 4(c) and 4(d)]. Figure 4(c) shows the simulated spectral absorption of detectors with various spacer thicknesses. The simulation results revealed obvious spacer thickness-dependent absorption peaks. The spectral enhancement ratio between detectors with and without resonant cavities was also experimentally measured and demonstrated ~200% enhancement in photoresponse [Figs. 4(d) and 4(e)]. It is worth noting that the addition of cavity layers did not degrade the noise level.

Therefore, the detectivity of the resonant cavity-enhanced detectors can be improved by a factor of 2, leading to enhanced detectivity up to ~8×10^{10} Jones at the fused-band mode and ~3.1×10^{11} Jones at the single-band mode, respectively.

4. CONCLUSIONS

Photodetection of light generated from different mechanisms (blackbody radiations, specularly reflected and transmitted light from objects) represents enormous and distinct optical information including thermal distribution, molecular composition, and surface texture. By fusing information on the detector level, fused images without registration error can be achieved, which is a great advantage over current image fusion methods with
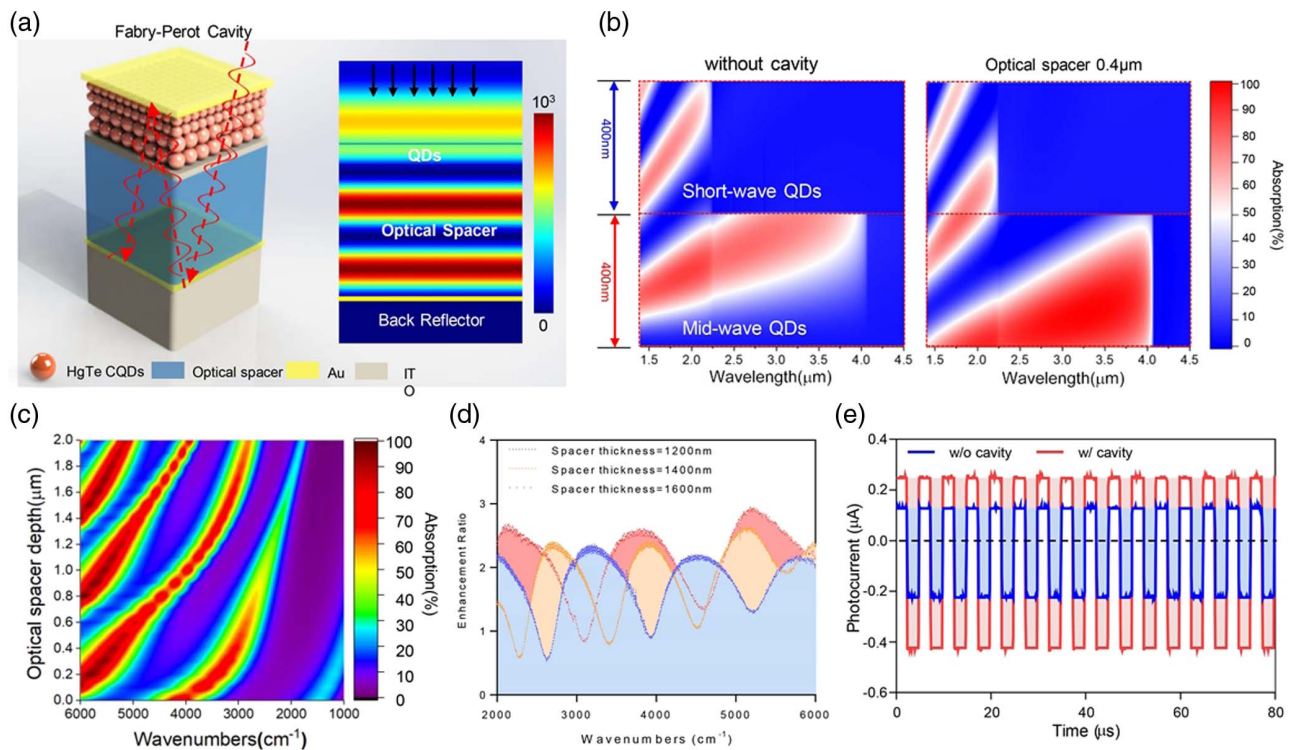
Fig. 4. Resonant cavity-enhanced dual-mode operation. (a) Illustration of resonant cavity structure. The inset on the right side is the simulated light *E*-field mapping in the cavity. (b) Simulated light absorption mapping in dual-mode detectors with and without a cavity. (c) Simulated spectral absorption at various spacer thicknesses. (d) Measured spectral enhancement ratio at various spacer thicknesses. (e) Photocurrents from dual-mode detectors with and without a cavity.

separate imagers. In this work, we constructed a dual-mode photodetector with three alternatingly stacked photodiodes, which exhibits remarkable dual-mode operation. By changing the polarity of bias voltage, the triple-junction detectors can be tuned between single-band detectors and fused-band detectors. The single-band mode detects short-wave infrared while the fused mode can detect and fuse photons from both short-wave and mid-wave infrared. Optical information from different spectral bands can be added together without post-processing or image algorithms. The addition of the middle diode with opposite polarity is the key to this unprecedented dual-mode operation by providing an interfacial carrier transport channel for fused-band response and single-band SWIR detection. The detectivity for the single-band SWIR mode and the fused-band SWIR/MWIR mode can be as high as 8×10^{10} Jones at the fused-band mode and $\sim 3.1 \times 10^{11}$ Jones at the single-band mode, respectively. The dual-mode detectors showed fast response with rising and fall times of 200 and 320 ns and the measured –3 dB bandwidth could be as high as 1.7 MHz. By switching bias polarity, dual-mode imaging and remote temperature sensing have been demonstrated, offering the potential to miniaturize dual-vision imaging systems. The dual-mode detectors provide night vision and thermal information-enhanced night vision imaging capability, and we believe it could be useful in the realization of advanced applications, including self-driving, surveillance, computer vision, and bio-medical imaging.

Author Contribution. X. T. conceived and designed the experiments. S. Z., G. M., and Y. L. fabricated the samples and performed data analysis. S. Z., Y. T., and P. Z. synthesized and characterized the colloidal materials. M. C. and Q. H. performed data analysis and contributed discussion of the operation mechanism. All authors contributed to discussions of the paper.

Disclosures. The authors declare no competing interests.

Data Availability. Data underlying the results presented in this paper are not publicly available at this time but may be obtained from the authors upon reasonable request.

†These authors contributed equally to this work.

REFERENCES

1. J. Ma, W. Yu, P. Liang, C. Li, and J. Jiang, "FusionGAN: a generative adversarial network for infrared and visible image fusion," Inf. Fusion **48**, 11–26 (2019).
2. J. Ma, J. Zhao, Y. Ma, and J. Tian, "Non-rigid visible and infrared face registration via regularized Gaussian fields criterion," Pattern Recogn. **48**, 772–784 (2015).

3. S. G. Kong, J. Heo, F. Boughorbel, Y. Zheng, B. R. Abidi, A. Koschan, M. Yi, and M. A. Abidi, "Multiscale fusion of visible and thermal IR images for illumination-invariant face recognition," Int. J. Comput. Vis. **71**, 215–233 (2007).

4. J. Ma, C. Chen, C. Li, and J. Huang, "Infrared and visible image fusion via gradient transfer and total variation minimization," Inf. Fusion **31**, 100–109 (2016).

5. M. V. Kovalenko, "Opportunities and challenges for quantum dot photovoltaics," Nat. Nanotechnol. **10**, 994–997 (2015).

6. S. Keuleyan, E. Lhuillier, and P. Guyot-Sionnest, "Synthesis of colloidal HgTe quantum dots for narrow mid-IR emission and detection," J. Am. Chem. Soc. **133**, 16422–16424 (2011).

7. S. Keuleyan, E. Lhuillier, V. Brajuskovic, and P. Guyot-Sionnest, "Mid-infrared HgTe colloidal quantum dot photodetectors," Nat. Photonics **5**, 489–493 (2011).

8. X. Tang, M. M. Ackerman, G. Shen, and P. Guyot-Sionnest, "Towards infrared electronic eyes: flexible colloidal quantum dot photovoltaic detectors enhanced by resonant cavity," Small **15**, 1804920 (2019).

9. M. M. Ackerman, X. Tang, and P. Guyot-sionnest, "Fast and sensitive colloidal quantum dot mid-wave infrared photodetectors," ACS Nano **12**, 7264–7271 (2018).

10. X. Tang, M. M. Ackerman, and P. Guyot-Sionnest, "Thermal imaging with plasmon resonance enhanced HgTe colloidal quantum dot photovoltaic devices," ACS Nano **12**, 7362–7370 (2018).

11. X. Wang, G. I. Koleilat, J. Tang, H. Liu, I. J. Kramer, R. Debnath, L. Brzozowski, D. A. R. Barkhouse, L. Levina, S. Hoogland, and E. H. Sargent, "Tandem colloidal quantum dot solar cells employing a graded recombination layer," Nat. Photonics **5**, 480–484 (2011).

12. J. Tang, X. Wang, L. Brzozowski, D. A. R. Barkhouse, R. Debnath, L. Levina, and E. H. Sargent, "Schottky quantum dot solar cells stable in air under solar illumination," Adv. Mater. **22**, 1398–1402 (2010).

13. A. K. Rath, M. Bernechea, L. Martinez, and G. Konstantatos, "Solution-processed heterojunction solar cells based on p-type PbS quantum dots and n-type Bi_2S_3 nanocrystals," Adv. Mater. **23**, 3712–3717 (2011).

14. J. Qu, M. Weis, E. Izquierdo, S. G. Mizrahi, A. Chu, C. Dabard, C. Gréboval, E. Bossavit, Y. Prado, E. Péronne, S. Ithurria, G. Patriarche, M. G. Silly, G. Vincent, D. Boschetto, and E. Lhuillier, "Electroluminescence from nanocrystals above 2 μm," Nat. Photonics **16**, 38–44 (2022).

15. A. Rogalski, "History of infrared detectors," Opto-Electron. Rev. **20**, 279–308 (2012).

16. A. Rogalski, J. Antoszewski, and L. Faraone, "Third-generation infrared photodetector arrays," J. Appl. Phys. **105**, 091101 (2009).

17. X. Tang, M. M. Ackerman, M. Chen, and P. Guyot-Sionnest, "Dual-band infrared imaging using stacked colloidal quantum dot photodiodes," Nat. Photonics **13**, 277–282 (2019).

18. S. Zhang, M. Chen, G. Mu, J. Li, Q. Hao, and X. Tang, "Spray-stencil lithography enabled large-scale fabrication of multispectral colloidal quantum-dot infrared detectors," Adv. Mater. Technol. **7**, 2101132 (2021).

19. E. H. Sargent, "Infrared photovoltaics made by solution processing," Nat. Photonics **3**, 325–331 (2009).

20. S. Sista, M. H. Park, Z. Hong, Y. Wu, J. Hou, W. L. Kwan, G. Li, and Y. Yang, "Highly efficient tandem polymer photovoltaic cells," Adv. Mater. **22**, 380–383 (2010).

21. J. Y. Kim, K. Lee, N. E. Coates, D. Moses, T. Q. Nguyen, M. Dante, and A. J. Heeger, "Efficient tandem polymer solar cells fabricated by all-solution processing," Science **317**, 222–225 (2007).

22. A. Hwang, M. Park, Y. Park, Y. Shim, S. Youn, C. Lee, H. B. Jeong, H. Y. Jeong, J. Chang, K. Lee, G. Yoo, and J. Heo, "Visible and infrared dual-band imaging via Ge/MoS_2 van der Waals heterostructure," Sci. Adv. **7**, eabj2521 (2021).

23. M. Dai, H. Chen, R. Feng, W. Feng, Y. Hu, H. Yang, G. Liu, X. Chen, J. Zhang, C. Xu, and P. Hu, "A dual-band multilayer InSe self-powered photodetector with high performance induced by surface plasmon resonance and asymmetric Schottky junction," ACS Nano **12**, 8739–8747 (2018).

24. J. Deng, L. Zong, W. Bao, M. Zhu, F. Liao, Z. Guo, Y. Xie, B. Lu, J. Wan, J. Zhu, R. Peng, and Y. Chen, "Integration of MoS_2 with InAlAs/InGaAs heterojunction for dual color detection in both visible and near-infrared bands," Adv. Opt. Mater. **7**, 1901039 (2019).

25. H. Kim, W. Kim, Y. Pak, T. J. Yoo, H. W. Lee, B. H. Lee, S. Kwon, and G. Y. Jung, "Bias-modulated multicolor discrimination enabled by an organic–inorganic hybrid perovskite photodetector with a p-i-n-i-p configuration," Laser Photon. Rev. **14**, 2000305 (2020).

26. Z. Lan, Y. Lei, W. Kin, E. Chan, S. Chen, D. Luo, and F. Zhu, "Near-infrared and visible light dual-mode organic photodetectors," Sci. Adv. **6**, eaaw8065 (2020).

27. B. Zhu, M. Chen, S. V. Kershaw, A. L. Rogach, N. Zhao, and H. K. Tsang, "Integrated near-infrared photodetector based on colloidal HgTe quantum dot loaded plasmonic waveguide," in *Conference on Lasers and Electro-Optics Pacific Rim (CLEO-PR)* (IEEE, 2017), pp. 1–3.

28. X. Tang, G. F. Wu, and K. W. C. Lai, "Plasmon resonance enhanced colloidal HgSe quantum dot filterless narrowband photodetectors for mid-wave infrared," J. Mater. Chem. C **5**, 362–369 (2017).

29. A. C. Arsenault, T. J. Clark, G. Von Freymann, L. Cademartiri, R. Sapienza, J. Bertolotti, E. Vekris, S. Wong, V. Kitaev, I. Manners, R. Z. Wang, S. John, D. Wiersma, and G. A. Ozin, "From colour fingerprinting to the control of photoluminescence in elastic photonic crystals," Nat. Mater. **5**, 179–184 (2006).

30. V. Reboud, N. Kehagias, M. Zelsmann, M. Striccoli, M. Tamborra, M. L. Curri, A. Agostiano, D. Mecerreyes, J. A. Alduncín, and C. M. S. Torres, "Nanoimprinted photonic crystals for the modification of the (CdSe)ZnS nanocrystals light emission," Microelectron. Eng. **84**, 1574–1577 (2007).